Ionospheric Plasma Irregularities During Intense geomagnetic storms of Solar Cycle 25

Nadia Imtiaz[1], Andres Calabia[2, 3], Chukwuma Anoruo[4], Aqsa Zahid[5], Christine Amory[6], and Binod Adhikari[7]

[1]Theoretical Physics Division, PINSTECH, Pakistan
[2]School of Surveying and Land Information Engineering, Henan Polytechnic University, Jiaozuo, China.
[3]Department of Physics and Mathematics, University of Alcalá, 28801-Alcalá de Henares (Madrid), Spain.
[4]Laboratório de Física e Astronomia, Universidade do Vale do Paraíba, Av. Shishima Hifumi, 2911–Urbanova, São José Dos Campos (SP), Brazil
[5]Department of Physics, Quaid-i-Azam University, Pakistan
[6]Plasmas (LPP), CNRS, Sorbonne Université, Université Paris Saclay, Observatoire de Paris, Ecole polytechnique, Institut Polytechnique de Paris, Paris, France, 3
[7]Department of Physics, Patan M. Campus, Tribhuvan University, Lalitpur, Nepal

Correspondence: Nadia Imtiaz (nhussain@ualberta.ca)

Abstract. This study aims to characterize several key aspects of the ionosphere during intense geomagnetic storms that occurred on March 23-25, 2023, April 23-25, 2023, November 4-7, 2023 and May 10-13, 2024 during the ascending phase of Solar Cycle 25 (SC25). We are especially interested in studying the role of asymmetric Joule Heating (JH) in the structuring of the Equatorial Ionization Anomaly (EIA), such as double crest, single crest, or merged, which may lead to the formation or suppression of post-sunset ionospheric plasma irregularities. For this purpose, we used the Weimer 2005 model simulations to analyze the JH patterns during the four strong geomagnetic storms, and Madrigal TEC maps are used to observe changes in the intensity, location, and symmetry of the EIA during these disruptive times. Equatorial/low-latitude ionospheric plasma irregularities at different longitudes under geomagnetically disturbed conditions are studied using the Rate of Change TEC Index (ROTI), which is calculated from GPS receiver measurements. A strong JH is observed during the May 2024 storm (also known as the Mother's Day storm) during its main phase, which occurs after sunset between 18:00 and 00:00 UT. The other storms have JH strength in the following order from strong to weak: March 2023, April 2023, and November 2023. In addition to interhemispheric asymmetry, all the storms show stronger variation in the JH patterns. We conclude that the resulting change in the thermospheric winds and electric fields due to storm conditions alters the EIA structures. It has been found that the generation of ionospheric plasma irregularities and their geographical distribution strongly depend on EIA's density gradients and general structure. For instance, it is noticed that the double crest EIA structures with strong plasma density gradients play an important role in the generation of post-sunset ionospheric plasma irregularities during the main phases of these geomagnetic storms. However, the single-crest or merged EIA structure comprises a diffuse region of high electron density centered directly over the equator, without a pronounced trough, as observed during the storm of November 2023. The single crest EIA exhibit nearly uniform plasma density distribution, do not favor the generation of ionospheric plasma irregularities. The role of a storm-time penetrating electric field in the structuring and seeding of ionospheric plasma irregularities has been

investigated. The research will contribute to our understanding of the basic physics of the ionosphere, especially the mechanisms governing the development and evolution of the EIA and ionospheric plasma irregularities under various magnetically disturbed conditions.

1   INTRODUCTION

25   The study of ionospheric properties, particularly the equatorial ionosphere, is critical because of its influence on radio signal transmission, such as those from Global Navigation Satellite Systems (GNSS). The ionosphere is an ionized region of the upper atmosphere that ranges from 60 to 1000 kilometers above the Earth's surface and is separated into three major regions: D (50-90 km), E (90-150 km), and F (150-500 km). These regions with lack of a clear boundaries exhibit diurnal and seasonal fluctuations, especially during magnetic storms, when changes in both thermosphere and ionospheric parameters such

30   as neutral wind, neutral composition, and ionospheric electric field deviate from their regular patterns, describing upper atmosphere variability (Balan et al., 2018), and generating significant disturbances in GNSS (Zhang et al., 2020). Ionospheric effects on applications are generally minor in mid-latitudes, causing only small perturbations in signal propagation that may be roughly expected, especially during magnetic storms. However, the equatorial region experiences more severe disturbances and irregular ionospheric structures. Storm-related variations in thermosphere/ionosphere parameters can dramatically alter the

35   low-latitude ionosphere phenomena, notably the equatorial plasma fountain (EPF), equatorial ionization anomaly (EIA) and ionospheric plasma irregularities (Kelly, 2009; Kassa et al., 2015). The EPF consists of two components: the upward drift force $E \times B$, which lifts the plasma to higher altitudes away from the magnetic equator, and the field-aligned diffusion of plasma along the magnetic field lines at all altitudes. The EIA is a feature of the non-uniform latitudinal distribution of ionospheric electron density caused by the upward $E \times B$ drift, with two crests at magnetic latitudes of about $15°$ north/south and a trough

40   near the magnetic dip equator (Balan et al., 2018). The EPF, the EIA, and the density gradients in the EIA would all be affected by the zonal electric fields. EPF variations may occur due to zonal electric fields during magnetic storms, which may also increase daytime eastward electric fields.

Storm-time electric fields can emerge from either a short-lived prompt penetration electric field (PPEF) caused by solar wind-magnetospheric interaction or a disrupted dynamo (DD) electric field. The southward turning of the IMF B_z component causes

45   a rapid increase in high-latitude convection and substorm activity. Convective electric fields at high latitudes can expand much faster than the magnetosphere can respond, which enables them to penetrate the low-latitude ionosphere. The PPEF polarity is eastward during the day and westward during the night. Additionally, the region 2 current builds up the shielding layer due to the enhanced convection, allowing an overshielding electric field opposite to the PPEF polarity to penetrate the low-latitude ionosphere when the IMF B_z turns northward. This penetration can be as efficient as when the IMF B_z turns South. The

50   DD electric field is a manifestation of disturbed thermospheric winds. Storm-time high-latitude heating enhances meridional neutral winds, resulting in strong equatorial winds. At low latitudes, these disturbance winds generate a westward/eastward electric field on the dayside and nightside, contradicting their quiet-time tendencies. Compared to the PPEF, the disturbance dynamo forms more slowly. Because of neutral air inertia, the disturbance winds and related dynamo electric fields take many

hours to form and may last for several hours (Astafyeva et al., 2018; Blanc and Richmond, 1980; Huang et al., 2005; Kikuchi
et al., 2008). Moreover, the equatorial vertical plasma drifts associated with the PPEF and DD exhibit seasonal and longitudinal
dependence (Fejer et al., 1999).

Aside from storm-time electric fields, the disturbed thermospheric equator-ward neutral wind can carry plasma from one hemisphere to the other and, depending on its amplitude and direction, alter the low-latitude ionosphere. Storm-time continuous
energy input in the high latitude ionosphere-thermosphere coupling system causes the neutral atmosphere to rapidly expand.
This growth can produce variations on the global distribution of the O/N2 ratio. Such disturbances in the neutral composition
also influence the EIA, either positively by increasing plasma density or negatively by reducing plasma density, depending on
the relative shift in O to N2 ratio distribution (Li et al., 2018; Rishbeth, 2000; Kassa et al., 2015). Thermosphere circulation
impacts the relative strength of EIA crests in the summer and winter hemispheres, leading to the EIA hemispheric asymmetry
(Huang et al., 2005; Tulasi et al., 2009). The trans-equatorial neutral wind from the summer to the winter hemisphere raises
electron density at the winter hemisphere's crest. Also, an increase in solar extreme ultraviolet (EUV) in January caused by a
decrease in the Sun-Earth distance at perihelion resulted in a 20% greater electron density in the northern EIA crest than in
the southern EIA crest (Lin et al., 2005). As mentioned above, the EIA is defined by two plasma density crests around $15°$
from the magnetic equator, is an important phenomenon in the ionosphere F region at low latitudes (Appleton, 1946; Balan
et al., 2018; Wu et al., 2023). The "fountain effect" created by vertical plasma drift and diffusion usually explains the formation
of EIAs. When combined with ambipolar diffusion, an eastward daytime dynamo electric field at the dip equator generates
an upward drift that lifts the ionospheric plasma to higher altitudes, resulting in two plasma density crests at $15°$ magnetic
latitudes in the ionospheric F region. Storm-induced perturbations in electric fields, neutral winds, and neutral composition all
affect EIA evolution during storms. The storm-time expansion in the EIA to mid-latitudes and considerable density changes are
caused by eastward PPEF and disturbed meridional winds (Balan et al., 2009; Tsurutani et al., 2004). Aside from double-crest
EIA, single-crest or merged EIA over or near the magnetic equator can also develop under certain ionospheric conditions. The
stronger (weaker) fountain effect, is responsible for the stronger (weaker) and extended (contracted) EIA crests. At low and
equatorial latitudes, a single crest may be observed if the two crests are suppressed by a weaker fountain effect. Huang et al.
(2013) studied that the single crest in the TEC over $110°$E longitude was primarily happened during periods of extremely
low solar activity. Balan et al. (2013) showed that the merging of the daytime EIA crests during the recovery phase (RP) of
several storms can be attributed to plasma convergence over the equator caused by equatorward storm-time neutral winds, with
minor contributions from downward $\boldsymbol{E} \times \boldsymbol{B}$ drift and an increase in O/N2 ratios. Here, we employ Madrigal TEC database to
examine the formation of single and double crest EIA structures under different physical conditions that occurred during the
ascending phase of the SC25.

Plasma depletions (or irregularities) are significant localized decreases in ionospheric F-region plasma density induced by the
development of a Rayleigh-Taylor (R-T) instability after sunset, which causes severe radio signal disruptions while passing
through them. The majority of plasma depletions occur in the EIA region (M et al., 2012). Vaggu et al. (2023) studied the
morphological and spectral aspects of ionospheric irregularities at E and F regions over Poker Flat using modeling and observations. Their analysis showed that the E-region irregularities extend along the magnetic field lines, with rod-shaped structures,

whereas the F-region irregularities have wing-like structures, with irregularities extending both along and across the magnetic
90 fields. It was also discovered that the spectral index or the power-law index of the E-region event is lower than that of the
F-region events. Furthermore, the spectral slope on the ground at higher frequencies is smaller than the spectral slope at irregularity height.

Previous studies have shown that geomagnetic storms of similar strength can frequently produce different ionospheric response. For instance, Aa et al. (2020) presented a statistical analysis of EPIs utilizing in situ plasma density observations
95 from the Swarm constellation from December 2013 to December 2019. The occurrence patterns of both post-sunset and post-midnight EPIs were explored in terms of longitude, season, local time, latitude, solar activity, and geomagnetic activity level.
The main results were as follows: (1) The occurrence frequencies of post-sunset/post-midnight EPIs showed varying longitudinal and seasonal dependence: The post-sunset EPIs showed the highest occurrence rate over the American-Atlantic sectors during the December solstices and equinoxes, whereas the post-midnight EPIs showed the highest occurrence rate during the
100 June solstices, particularly over the African sector. (2) Post-sunset EPI occurrence rates were positively correlated with solar activity, but post-midnight EPIs were adversely correlated. (3) The latitudinal distribution of EPIs showed a double-peak pattern about $\pm 5°$ magnetic latitude, with a higher peak in summer. (4) As geomagnetic activity increases, so does the occurrence of EPIs. (5) The magnetic declination angle, equatorial vertical $\boldsymbol{E} \times \boldsymbol{B}$ drift, and thermospheric zonal wind are the primary factors influencing the distribution of EPIs after sunset. The key governing factors for post-midnight EPIs are thought to be
105 atmospheric gravity waves and equatorially directed thermospheric meridional wind associated with the midnight temperature maxima.

The complex interaction of the magnetosphere, ionosphere, and thermosphere causes variations in ionospheric disturbances from storm to storm. These disturbances are more noticeable and frequent at night, when high-latitude energy injection occurs and neutral winds favor an equatorial direction (Fuller-Rowell et al., 1997). In low-latitude and equatorial regions, intense
110 geomagnetic storms can create ionospheric plasma irregularities, which are most noticeable at night. Storm-time uplift of the ionospheric F-layer increases the likelihood of RT instability-induced plasma irregularities near the magnetic equator after sunset. These irregularities can be as small as a few centimeters or as large as thousands of kilometers (Abdu et al., 2009).
The vertical $\boldsymbol{E} \times \boldsymbol{B}$ plasma drift and the strong plasma density gradient near equator can cause gravitational RT-instability in the nighttime ionosphere, leading to post-sunset plasma irregularities at equatorial/low latitudes (González, 2022; Calabia
115 et al., 2024; Imtiaz et al., 2024; Tahir et al., 2024; Kassa et al., 2024). Eastward (westward) storm time electric fields can create favorable (unfavorable) conditions for irregularity generation (suppression) by raising (lowering) the F-region ionosphere near the magnetic equator. Pre-reversal enhancement (PRE) in the $\boldsymbol{E} \times \boldsymbol{B}$ drift can cause an uplift of the F-layer which can provide ideal conditions for the formation of irregularities via RT-instability. Studies showed that the strong storm-time drivers can increase or decrease the vertical $\boldsymbol{E} \times \boldsymbol{B}$ drift that may initiate or suppress the ionospheric plasma irregularities during a
120 storm (Aarons, 1991, 1997; Tulasi et al., 2009). The vertical transport of plasma, which is primarily responsible for irregularity formation, occurs due to the effect of a zonal electric field generated by dynamo action inside the ionosphere or an electric field imposed from the magnetosphere (Abdu, 2020). The suppression of ionospheric plasma irregularities could be attributed to a westward PPEF of magnetospheric origin caused by northward IMF B_z, as well as DD caused by storm-induced equatorial

winds (Huang et al., 2013; Kassa et al., 2023; Imtiaz et al., 2024; Kassa et al., 2024). In this context, Huang (2019) reported
that the presence of the long term eastward penetration electric field in the equatorial ionosphere, enhanced vertical ion drift
in the upward direction by up to 180 m/s. Wu et al. (2023) used MAGE simulations and ICON IVM observations to show that
eastward/westward electric field lead to upward/downward ion drifts during the geomagnetic storm of November 3-4, 2023.
Multiple factors, including solar and geomagnetic activity, latitude and longitude, local time, and season, influence ionospheric
irregularities (Abdu, 1997; Dugassa et al., 2019). To better understand their variability, it is necessary to analyze the occurrence
characteristics of ionospheric plasma irregularities under different geomagnetic conditions.

In this study, we investigate different storm-time ionospheric conditions that characterize the structural forms of the EIA,
leading to post-sunset plasma irregularities. For this purpose, we use madrigal TEC maps to study the EIA features such as
separated or merged crests after sunset during the main phases of the intense geomagnetic storms of the 25th solar cycle.
The GNSS based ROTI is used to study the post-sunset ionospheric irregularities during magnetically disturbed conditions.
In addition, PPEF observations are used to investigate the role of low-latitude ionospheric electric field in the formation of
different structures of the EIA which are favorable for R-T instability to generate ionospheric plasma irregularities. The article
is organized as follows: Section 2 describes the data and analysis approach, whereas Section 3 presents the results and their
interpretations. Finally, Section 4 presents our findings and conclusions.

2 DATASETS and MODELS

We use 1-minute and hourly time-resolution data of solar wind parameters such as the B_z component of the interplanetary
magnetic field (IMF), the solar wind speed (V_{sw}), the eastward zonal component E_y of the interplanetary electric field (IEF),
the ring current proxy index ($SYM - H$), the geomagnetic activity index (Kp), and the solar radio flux at 10.7 cm (F10.7). The
data can be found at https://omniweb.gsfc.nasa.gov/form/omni_min.html in the NASA OMNIWeb database.

The Community Coordinated Modeling Center (CCMC) hosted Weimer-2005 model driven by ACE solar wind data is used to
study the high-latitude ionospheric electrodynamics (Weimer, 2005). It is an improved empirical model to compute magnetic
field-aligned currents (FACs) and high-latitude electric potentials as a function of solar wind properties. As an analog of the
electric potential model, the FAC model is constructed using scalar magnetic Euler potentials. The potentials are constructed
from several Fourier series functions of longitude at discrete latitudinal intervals at lower latitudes. Joule heating (JH) and total
Poynting flux in the ionosphere can be calculated using the FAC and electric potential models. Since the FAC model implicitly
incorporates the conductivity variations as a function of solar tilt, ionospheric currents and JH can be derived without the need
for a separate model of ionospheric conductivity.

Worldwide TEC maps, updated every 5 minutes, are available in the CEDAR Madrigal database. The maps have a spatial
resolution of $1° × 1°$ for geographic latitude (GLAT) and longitude (GLON). The data is sourced from ground-based GNSS
signals, which are publicly available at http://cedar.openmadrigal.org/. Rideout and Coster (2006) provides a comprehensive
understanding of data processing techniques of these maps.

The Rate of Total Electron Content Index (ROTI), which interprets the TEC's variability over time, is an indicator of iono-

Table 1. Information about the location and local time (LT) of GNSS stations used in the analysis.

Instrument	Station	Sector	Geographic (Latitude, Longitude)	Geomagnetic (Latitude, Longitude)	Local Time (LT)
GNSS	BAKO	Asia	$(6.49°S, 106.85°E)$	$(16.13°S, 179.93°W)$	UT+7
–	DGAR	–	$(6.49°S, 72.37°E)$	$(14.94°S, 143.93°W)$	UT+5
–	IISC	–	$(13.02°N, 77.57°E)$	$(4.87°N, 150.96°W)$	UT+5
–	CUSV	–	$(13.74°N, 100.53°E)$	$(4.39°N, 173.37°W)$	UT+7
–	HKSL	–	$(22.37°N, 113.93°E)$	$(13.19°N, 173.15°W)$	UT+7
–	RABT	Africa	$(34.1°N, 6.50°W)$	$(23.88°N, 69.23°E)$	UT+0
–	YKRO	–	$(6.86°S, 5.24°W)$	$(10.92°N, 68.67°E)$	UT+0
–	ABPO	–	$(19.02°S, 47.23°E)$	$(23.49°S, 116.71°E)$	UT+3
–	BOGT	America	$(4.64°N, 74.08°W)$	$(14.31°N, 1.46°W)$	UT-5
–	RIOP	–	$(1.65°S, 78.65°W)$	$(7.23°N, 6.46°W)$	UT-5
–	CORD	–	$(31.53°S, 64.47°W)$	$(22.43°S, 7.27°E)$	UT-4
–	SANT	–	$(33.15°S, 70.67°W)$	$(23.77°S, 1.83°E)$	UT-5

spheric irregularities (Aarons, 1997; Basu et al., 1999; Pi et al., 1997). GNSS-TEC software by (Seemala, 2011) solves for receiver biases and estimates the TEC from satellites with elevation angles $\geq 30°$ to minimize multi-path errors. Given TEC data at discrete intervals, the rate of change of TEC (ROT) can be computed as:

$$\text{ROT}(t_i) = \frac{\text{dTEC}}{\text{dt}} = \frac{TEC(t_{i+1}) - TEC(t_i)}{t_{i+1} - t_i}. \tag{1}$$

In this equation, dTEC is the difference between $\text{TEC}(t_{i+1})$ and $\text{TEC}(t_i)$ values at times t_{i+1} and t_i, respectively. ROTI is then calculated as the standard deviation of ROT over a specified period, usually 5 minutes,

$$\text{ROTI} = \sqrt{<\text{ROT}^2> - <\text{ROT}>^2}, \tag{2}$$

Table 1 shows the geographic and geomagnetic coordinates of equatorial and low-latitude GNSS receivers in the Asian, African, and American sectors, which are used to examine the temporal patterns of ROTI. For the categorization of ionospheric irregularities, we used ROTI values as follows: a ROTI value of less than 0.25 TECU/min indicates the absence of irregularities; a weak irregularity is identified when ROTI ranges from 0.25 to 0.5 TECU/min; a moderate irregularity is noted when ROTI falls between 0.5 and 1 TECU/min; and a strong irregularity is present when ROTI exceeds 1 TECU/min.

The temporal profile of the equatorial electric field over a particular longitude is obtained from the real-time Prompt Penetration Electric Field (PPEF) model, available at: https://geomag.colorado.edu/online-calculators/real-time-model-ionospheric-electric-fields. Employing real-time solar wind data and a climatological model for quiet conditions, the model calculates the temporal variation of the equatorial ionospheric eastward electric field (EEF) using a transfer function. Time and longitude are the inputs, and the outcomes are the total electric field (QP), i.e., the sum of background quiet-time electric field (Q) and the PPEF.

Table 2. Information about the Sudden Storm Commencement (SSC), the main phase end (MPE), the minimum values of the SYM-H index, the number of Sun spots (R), and Quiet days (Q) during different geomagnetic storms of the solar cycle 25.

Event	SSC	MPE	$SYM-H_{min}$	R	Q days
March 23-25, 2023	March 23 at 6:32 UT	March 24 at 5:21 UT	-170 nT	150	March 17-19
April 23-25, 2023	April 23 at 8:56 UT	April 24 at 4:03 UT	-233 nT	80	April 20-22
November 4-6, 2023	November 4 at 17:40 UT	November 5 at 16:54 UT	-189 nT	91	November 1-3
May 10-13, 2024	May 10 at 17:15 UT	May 11 at 02:14 UT	-518 nT	200	May 7-9

The information given in this table is obtained from OMNI web database.

3   RESULTS AND DISCUSSION

3.1   SOLAR AND MAGNETOSPHERE CONDITIONS

The investigation of the ionospheric response to geomagnetic storms reveals insight into the complex interplay between solar activity and Earth's atmosphere. In order to achieve this, we investigate four geomagnetic storms that occurred during the ascending phase of Solar Cycle 25. Figures 1-4 show (a) the B_z component of the IMF, and the solar wind speed (V_{sw}), (b) the zonal component eastward E_y of the IEF, and the ring current proxy index ($SYM-H$), and (c) the geomagnetic activity index (Kp), and the solar radio flux at 10.7 cm (F10.7) during the storm events considered. Information about the sudden storm commencement (SSC), the end of the main phase (MP), the minimum values of the SYM-H index, the number of Sun spots (R) and the magnetic quiet days (Q) during different geomagnetic storms is also given in Table 2. Following is a brief overview of the geomagnetic conditions during these events:

March 23-25, 2023 storm: As shown in Figure 1a, the IMF B_z makes two large southward turns throughout the main phase of the storm. The first southward turn occurs on March 23, at approximately 6:32 UT. Between 6:32 and 12:00 UT, the value of IMF B_z decreased from 2 to -10 nT. The second long-term southward turn in IMF B_z is seen on March 23, at 17:22 UT. During this turn, the IMF B_z value decreased from 10 nT to approximately -18 nT. The IMF B_z remains southward for approximately 9 hours before increasing around 5:21 UT on March 24. During the main phase of this storm, the V_{sw} fluctuated between 400 and 500 km/s. During the recovery phase of this storm, the V_{sw} increased and reached the maximum value of 600 km/s on March 25. A northward IMF B_z generates an electric field westward during the day and eastward at night. Figure 1 b shows that the IEF E_y reached about 4 mV / m after the first southward excursion of the IMF B_z. From 12:00 to 18:00 UT, on March 23, it fluctuated rapidly between +5 and -5 mV/m. During the second southward excursion, it again increases and reached the maximum value of 8.22 mV/m at 17:22 on March 23. After that, it started decreasing down to normal conditions. Figure 1c shows that the main phase of this storm started soon after SYM-H reached a value of 28 nT at the time of SSC. During the extended southward turning of IMF B_z ($B_z < 0$), enhanced ring current caused by magnetic reconnection dropped the SYM-H index to -170 nT on March 24, at 5:21 UT (end of the main phase). The SYM-H increases during the recovery phase until it reached the quiet time value. Figure 1 c shows that before SSC, Kp was less than 4+. On March 24, around 04:00 UT, the Kp value peaked at 8+ and then began to decrease as the storm recovery began around 5:21 UT. The F10.7 index
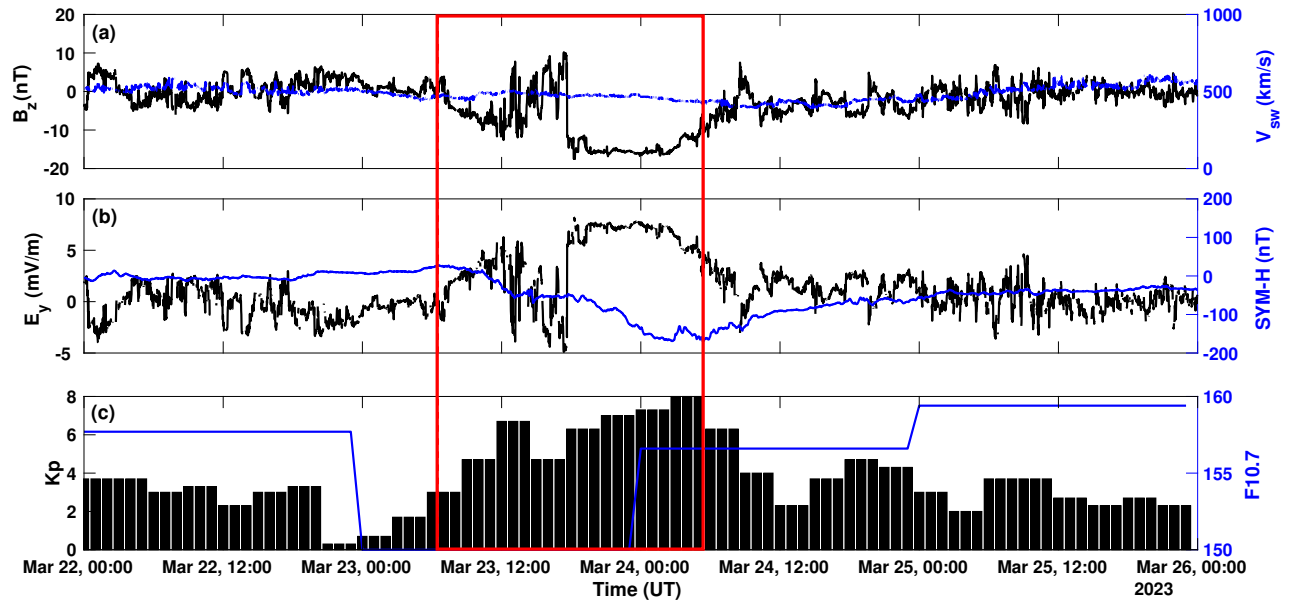
Figure 1. Temporal variation of: (a) solar wind speed (V_{sw}) and B_z component of IMF, (b) E_y component of IMF and $SYM - H$, and (c) the magnetic index (K_P) and the solar radio flux at 10.7 cm (F10.7) during March 22-25, 2023 storm.

fluctuated between 157.7 and 159.4 sfu during this period. As a result, variations in solar irradiance are expected to have little
200   impact on thermospheric composition during the storm.

April 23-25, 2023 storm: Figure 2(a-c) shows the solar wind and geomagnetic conditions during the period April 22-26,
2023. The interval between the vertical red lines indicates the main phase of the storm, starting at SSC on April 23 at 8:56
UT. At the time of the SSC, the IMF B_z is at 0 nT which turned southward, and then later reached to the value of -20 nT
between 18:00 UT to 21:00 UT. During this time, the V_{sw} increased from 400 km/s and reached to the maximum value of
205   751 km/s at 21:39 UT on April 23. After 3 hours, the IMF B_z turned northward and fluctuated between 0 nT and 20 nT until
01:20 UT before a second strong southward excursion on April 24. This second long-term southward turn in IMF B_z is seen
on April 24 at 1:21 UT. During this turn, a sharp decrease in the IMF B_z value from 20 nT to around -34 nT is observed as
shown in Figure 2a. The IMF B_z remains southward for approximately 3 hours until the end of the main phase at 4:03 UT on
April 24. During this period, the V_{sw} kept at approximately 600 km/s until the main phase ended at 4:03. Figure 2b shows
210   a two-step geomagnetic storm, with SYM-H minima values of -179 nT (at 21:59 UT) and -233 nT (at 04:03 UT) on April
23 and 24, respectively. During the main phase, the IEF E_y oscillates rapidly between -21 and 21 mV/m. During the solar
wind-magnetosphere interaction process, the Kp index increased to 8.3, indicating an intense geomagnetic storm conditions.
Following the strong geomagnetic storm, the Kp index dropped from 8.3 to 6.7, then surged to 8, before returning to a calm
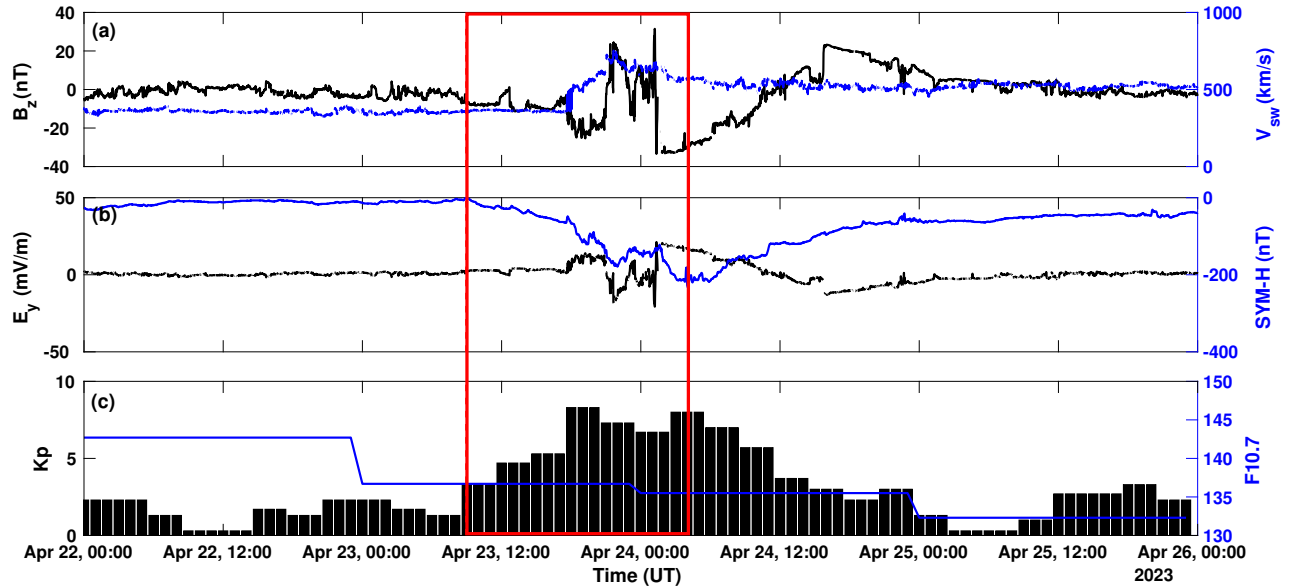
Figure 2. Temporal variation of: (a) solar wind speed (V_{sw}) and B_z component of IMF, (b) E_y component of IMF and $SYM - H$, and (c) the magnetic index (K_P) and the solar radio flux at 10.7 cm F10.7 during April 22-25, 2023 storm.

state. During this time, the solar activity level F10.7 remained steady at approximately 135 sfu as shown in Figure 2c. The
recovery phase began with the northward turning of the IMF B_z and returned to the 0 nT after 24 h. During recovery phase,
the V_{sw} also gradually decreased to normal conditions.

November 4-7, 2023 storm: The main phase of this storm began with a southward turning of the IMF B_z, reaching to
a lowest value of approximately -24.9 nT at 11:31 UT on November 5. Then at 12:00 UT it turned northward and reached
maximum value of approximately 40.1 nT at 13:56 UT on the same day. Afterwards, the IMF B_z shows a second long-term
southward turn reaching -20 nT until the end of the main phase at 16:54 UT. The B_z component increased gradually to normal
values on November 5. During the main phase, the V_{sw} is at moderate level around 500 km/s and it increased to 600 km/s at
12:00 UT on November 6. Figure 3 (b) shows the IEF E_y and SYM-H, correspondingly. During the compression phase, the
SYM-H sharply increased to 23 nT at 17:09 UT on November 4 and shortly after this the main phase of the storm begins with
decrease in SYM-H. It was also a double step storm with minimum values of SYM-H of approximately -100 nT (at 12:00 UT)
and -189 nT (at 16:54 UT) observed on November 5. Following the polarity of the IMF B_z, the IEF Ey also show fluctuations
between -19.5 and 10.5 mV/m. The solar radio flux remained in the range $140 < F10.7 < 160$ sfu during this period. Before
the SSC, Kp was less than 3+, indicating the quiet conditions, but as the storm begins, it rapidly increased to 5+ due to the
initial effect of solar wind shock at 17:40 UT on November 4. From 00:00 to 08:00 UT on November 5, the Kp decreased to
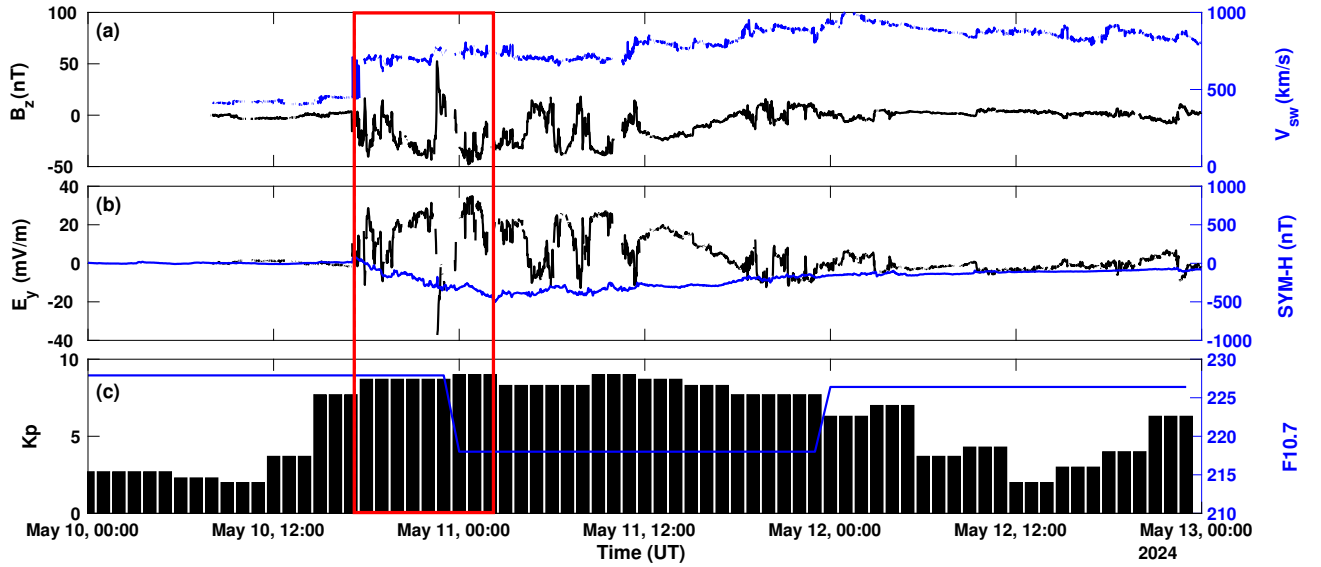
9
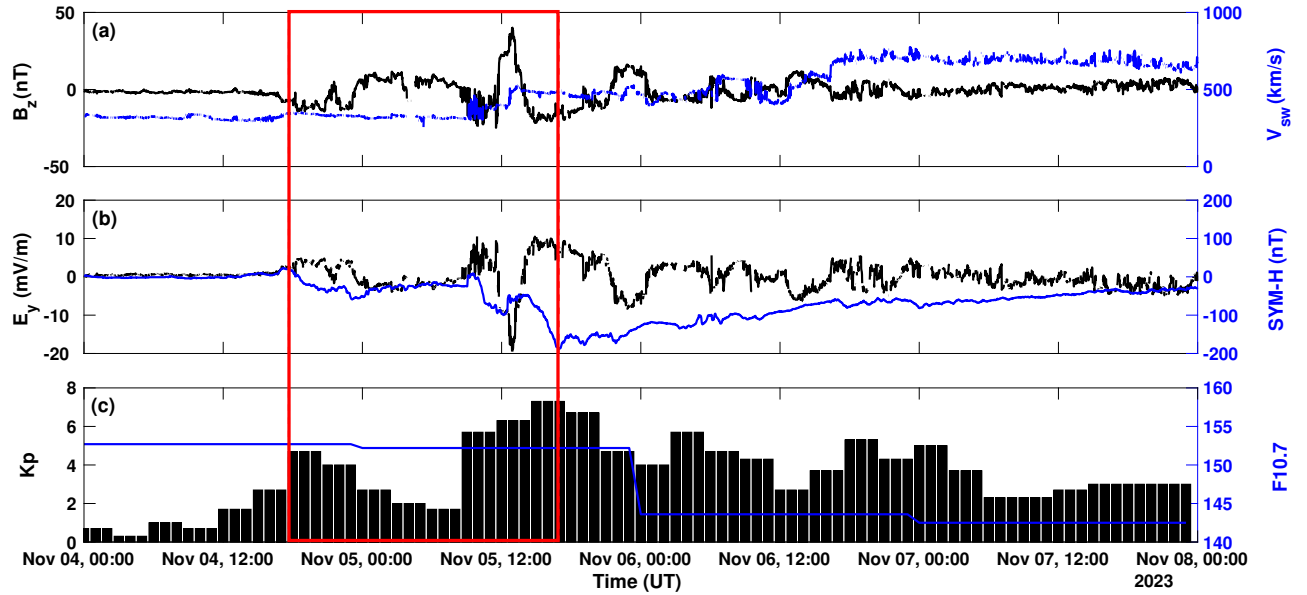
Figure 3. Temporal variation of parameters shown as: (a) solar wind speed (V_{sw}) and B_z component of IMF, (b) E_y component of IMF and SYM − H, and (c) the magnetic index (K_P) and the solar radio flux at 10.7 cm (F10.7) during November 4-7, 2023.

normal levels before rapidly increasing to 7+, predicting an intense geomagnetic storm between 12:00 UT and 19:00 UT on

230   November 5. The recovery phase started at 16:54 UT with a northward turning of the IMF B_z on November 5.

May 10-13, 2024 storm: Figure 4a displays the temporal changes in V_{sw} and the IMF B_z during May 10 to 13, 2024. The main phase began around 17:15 UT on May 10, with a sharp southward swing in the IMF B_z, reaching -30 nT, and an increase in V_{sw}, reaching around 700 km/s. Figure 4b shows variations in SYM-H and IEF E_y between May 10 and 13. Initially, the SYM-H index increases sharply to 88 nT as the Earth's magnetosphere compresses at 17:15 UT on May 10. Following this

235   initial increase, the main phase begins with a reduction in the SYM-H due to increased ring current in the magnetosphere. The main phase lasted until 02:14 UT on May 11, when the SYM-H index reached a maximum low of roughly -518 nT. During this phase, the IEF E_y fluctuates rapidly between -37 and 35 mV/m. The Kp index indicated substantial geomagnetic activity on May 10 between 12 and 15 UT, reaching a value of 5. Shortly after the SSC, Kp reached to 8 and then began fluctuating between 8 and 9 until the main phase ended at 02:14 UT on May 11. The solar activity level F10.7 stayed around 220 and 226

240   sfu as shown in Figure 4c. Following the storm recovery, the IMF B_z shows rapid north-south oscillations while the SYM-H increases gradually to reach the normal level. During this phase, the V_{sw} increased to 998 km/s and the Kp index varied between 7 and 9 until late evening on May 11.

Figure 4. Temporal variation of: (a) solar wind speed (V_{sw}) and B_z component of IMF, (b) E_y component of IMF and $SYM - H$, and (c) the magnetic index (K_p) and the solar radio flux at 10.7 cm (F10.7) during May 10-13, 2024.

3.2 High-Latitude Ionosphere

During geomagnetic storms, an increased convective electric field and the massive injection of high-energy particles result in an

245 increase in Pederson currents and ionospheric conductivity (Buonsanto, 1999; Lukianova, 2020; Dungey, 1961; Axford, 1964). This leads to an increase in the energy dissipation or Joule heating (JH), particularly in the Auroral zone where precipitation of high-energy particles occurs. Enhanced Joule heating at auroral latitudes expands the neutral atmosphere, driving equatorial neutral wind and generating traveling atmospheric/ionospheric disturbances (Richmond and Matsushita, 1975; Fuller-Rowell et al., 1994). In order to estimate the solar wind energy dissipated into the inner magnetosphere-ionosphere (MI) system

250 through JH during the four severe geomagnetic storms SC25, we used the CCMC-hosted Weimer 2005 model. The quiet time JH value varies from 1 to 10 $\mathrm{mW/m^2}$. However, the value of JH increases significantly during magnetically disturbed periods. During the main phase of each storm, the values of JH after sunset between the time 18:00 to 00:00 UT are given in Table 3 and also shown in Figure 5. For the geomagnetic storm of March 23 to 25, 2023, JH values showed notable inter-hemispheric asymmetries, with higher values in the southern hemisphere during the main phase. This storm was marked by

255 significant solar wind and IMF B_z fluctuations, with IMF B_z turning southward to -20 nT and V_{sw} peaking at 600 km/s during the recovery phase. The geomagnetic storm from April 23 to 25, 2023, exhibited significant IMF B_z and V_{sw} fluctuations,
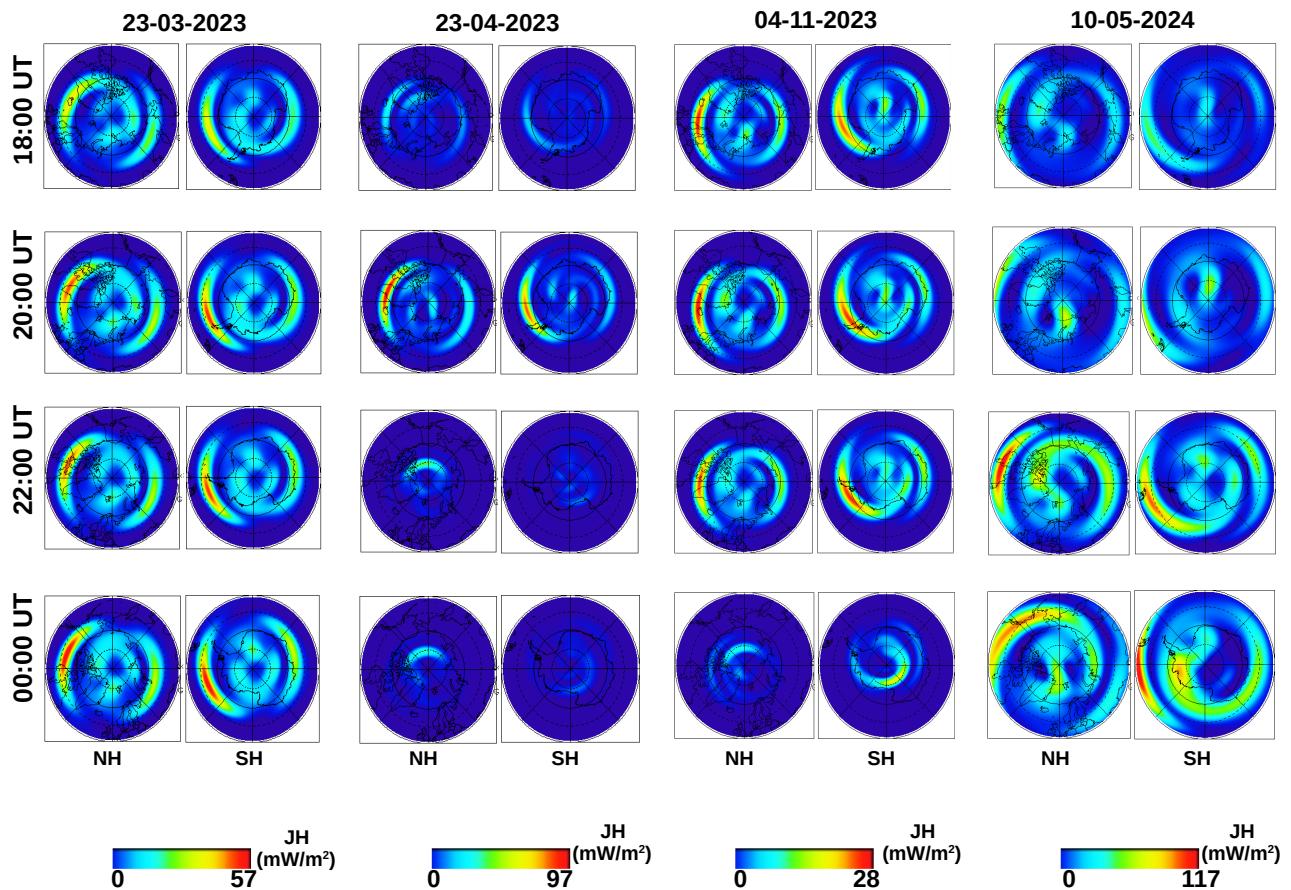
Figure 5. Polar maps of Joule heating from the Weimer 2005 Model computed at CCMC during the main phase of the four geomagnetic storms after sunset, from 18:00 UT to 00:00 UT.

leading to a two-step storm with SYM-H minima of -179 nT and -233 nT. JH values during this period showed significant inter-hemispheric asymmetries, with higher values in the northern hemisphere, particularly at 19:00 UT and 20:00 UT on April 23. The November 5-7, 2023 storm had notable IMF B_z fluctuations, with the V_{sw} increasing to 600 km/s during the main phase. JH values during this storm were relatively balanced between the hemispheres, with slight variations observed at different times. The May 10-13, 2024 storm was particularly intense, with the IMF B_z reaching -30 nT and the V_{sw} peaking at 700 km/s. JH values during this storm were significantly higher, especially in the northern hemisphere, with a peak of 114.7 mW/m^2 at 22:00 UT on May 10, indicating extreme geomagnetic activity and substantial energy dissipation in the ionosphere. In short, a strong JH is recorded during the main phase of the May 2024 storm from 18:00 to 00:00 UT. The order of JH after sunset from 18:00 to 00:00 UT is the following: May, March, April, and November. The inter-hemispheric asymmetries in the JH during distinct geomagnetic storms are caused by differences in heating between the northern and southern hemispheres. Factors such as Earth's magnetic dipole tilt, magnetic field geometry, seasons, and the orientation of the IMF, in particular the

IMF B_y (east-west component), all contribute to the JH's inter-hemispheric asymmetry (Smith et al., 2023). The storm-time Joule heating in high-latitude can cause atmospheric gravity waves (AGWs) to move equatorward, thus providing favorable
270 conditions for formation equatorial/low-latitude ionospheric plasma irregularities (H Jin, 2022).

3.3 Low-Latitude Ionosphere Response

During magnetic storms, the low latitude ionosphere exhibits different features due to the complicated interplay of geomagnetic activity, solar radiation, and ionospheric dynamics. Some of these features are discussed here:

3.3.1 Structure of Equatorial Ionization Anomaly (EIA)

275 Figure 6 (a-f) show the temporal variation of the ionospheric TEC during the main phase of the March 23-24, 2023 geomagnetic storm after sunset, from 18:00 UT to 00:00 UT. During the March 23-25, 2023 storm, TEC values showed notable inter-hemispheric asymmetries, with higher values in the southern hemisphere during the main phase. Initially, well-separated double crests in the EIA were observed, but merging of these crests occurred between 18:00 and 20:00 UT, leading to increased TEC in the equatorial zone. This merging and subsequent increase in TEC were driven by enhanced JH and geomagnetic activ-
280 ity. At the same time, the TEC began to gradually increase in the northern hemisphere. This increase continued, and by 20:00 UT, TEC values were higher in the northern hemisphere than in the southern hemisphere. It is also observed that in the southern hemisphere, the TEC anomalies are confined to low latitudes and they extend to mid-latitudes in the northern hemisphere. At 22:00 UT, the TEC decreases in the equatorial zone which again leads to the formation of the double crests in the EIA. On March 24, from 00:00 UT to 06:00 UT, high TEC values were observed at equatorial and low latitudes, indicating geomagnetic
285 disturbances towards the Asian sector. At 12:00 UT, the double crest in the northern hemisphere became a single crest, and TEC values slightly decreased. Starting from 14:00 UT, ionospheric TEC values began to increase again, marking the beginning of a second phase of ionospheric irregularities. The increase in TEC values towards the northern hemisphere indicated a period of geomagnetic disturbance until 22:00 UT. The decreasing TEC values are observed during the recovery phase of the geomagnetic storm from 06:00 UT onwards (See supporting Figure of madrigal TEC maps for March 23-24, 2023).
290 Figure 6 (g-i) depicts the temporal evolution of the ionospheric TEC during the strong geomagnetic storm of April 23-24, 2023. The April 23-24, 2023 storm exhibited well-defined double crests in the EIA on April 23, with TEC increasing in the EIA crests over America and expanding poleward due to strong JH. After achieving the peak value for the day, the TEC begins to decrease from 22:00 UT forward. The EIA's strength and latitudinal range had significantly decreased, as evidenced by the global ionospheric TEC distribution on April 24. The main phase of this geomagnetic storm terminates at 04:00 UT, with the
295 EIA's double crest over the southern hemisphere decreasing to a single crest (See the supporting Figure of madrigal TEC maps for April 23-24, 2023). Following the peak TEC value in the southern crest, a recovery phase begins at 4:03 UT and persisted until 22:00 UT. During the recovery phase, the ionospheric TEC returns to normal state.

Figure 6 (m-r) shows ionospheric TEC maps during show the temporal variation of the ionospheric TEC during the main phase of the November 4-5, 2023 geomagnetic storm after sunset, from 18:00 UT to 00:00 UT. The November 4-5, 2023 storm saw
300 storm-time ionization initially confined to the equatorial region, resulting in underdeveloped EIA crests. However, by 20:00
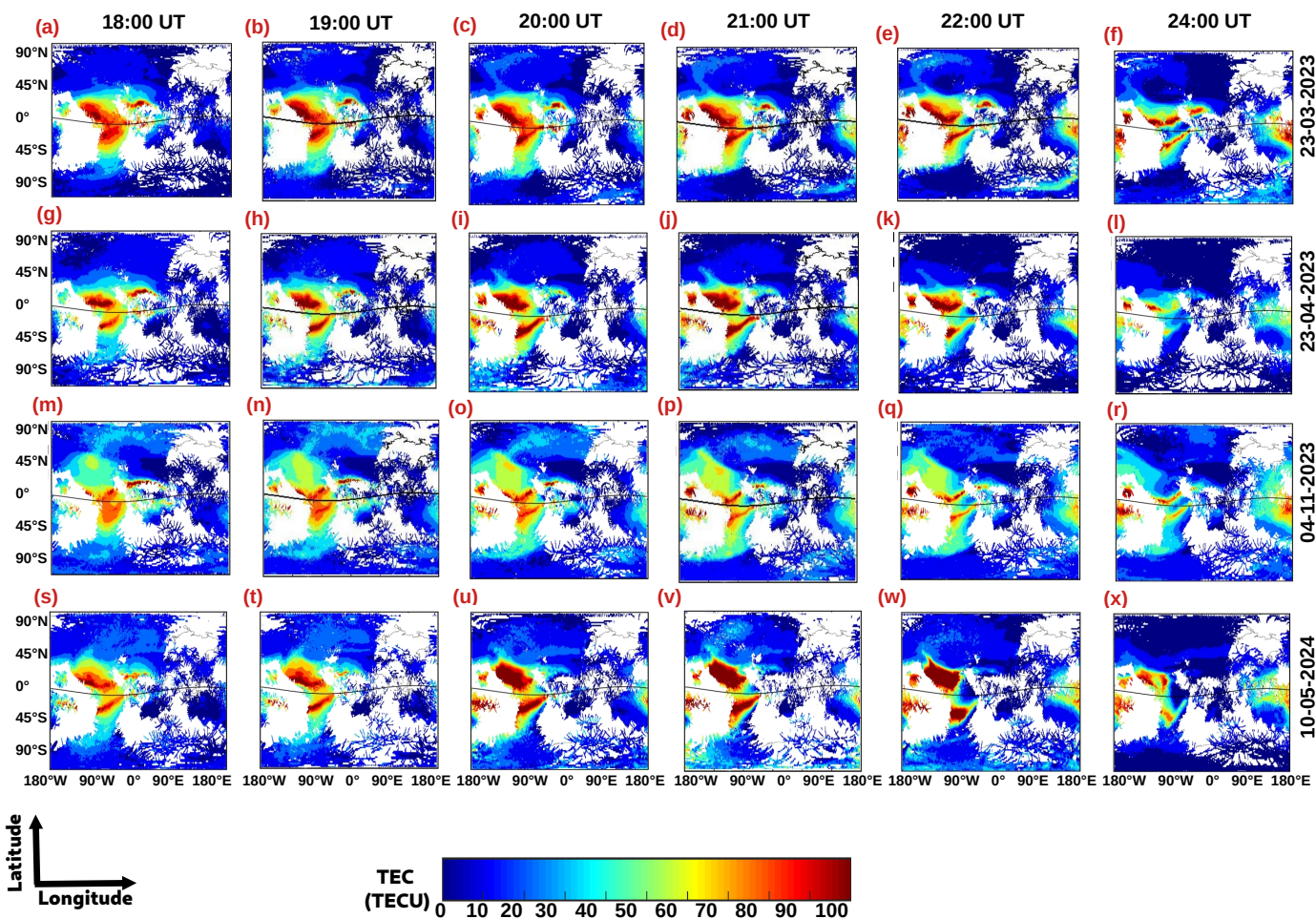
Figure 6. Madrigal-based global ionospheric TEC maps during the main phase of the four geomagnetic storms after sunset, from 18:00 UT to 00:00 UT shown as: (a-f) March 23-24, 2023, (g-l) April 23-24, 2023, (m-r) November 4-5, 2023, and (s-x) May 10-11, 2024.

UT, ionization increased in the northern and southern low latitudes, forming a weak EIA with smaller latitudinal extent.
On May 10, 2024, a double crest EIA structure at the equator containing normal TEC values with minor variations observed in other regions until 18:00 UT (See the supporting Figure of madrigal TEC maps for May 10-11, 2024). The global ionospheric maps in Figure 6 (s-x) illustrate the temporal variation of the ionospheric TEC during the main phase of the May 10-11, 2024 geomagnetic storm after sunset, from 18:00 UT to 00:00 UT. The May 10-11, 2024 storm was particularly intense, with substantial increases in TEC in the EIA crests over American longitudes and significant poleward shifting of the EIA crests up to about ±35° geomagnetic latitudes, associated with an external fountain effect. The recovery phase shows negative phase of this storm with a strong reduction in TEC along with EIA crests suppression and merging into a single equatorial band (See the supporting Figure of madrigal TEC maps for May 10-11, 2024). In each case, the variations in TEC were influenced

310 by the intensity and duration of geomagnetic activity, driven by solar wind parameters and enhanced JH, which affected the distribution and magnitude of ionospheric disturbances.

3.3.2   Ionospheric Plasma Irregularities

Figures 7-10 show temporal profiles of ionospheric plasma irregularities in the three longitudes that are America, Africa, and
315 Asia during the 4 geomagnetic storms. Each storm's unique solar wind conditions, geomagnetic activity, and JH distribution influenced the extent and location of ionospheric disturbances and plasma bubbles. During the March 23-25, 2023 storm, strong post-sunset plasma irregularities were observed in low/equatorial latitude stations (BOGT and RIOP) in the American sector, driven by significant solar wind and IMF B_z fluctuations, and enhanced JH. In contrast, the April 23-25, 2023 storm also showed post-sunset plasma irregularities over the same stations, but no irregularities were noted in other regions, highlighting the
320 localized impact of JH and geomagnetic activity. The November 4-6, 2023 storm saw highly suppressed post-sunset ionospheric plasma irregularities across all sectors due to lower ionospheric conductivity and weak electric fields, which reduced vertical plasma drifts and prevented irregularities from growing. The severe May 10-13, 2024 storm had a significant impact on the ionosphere, causing pronounced post-sunset plasma irregularities, particularly over southern low latitude stations (CORD and SANT) in the American sector. This was due to JH's inter-hemispheric asymmetry, where greater JH in the northern hemisphere
325 led to the penetration of atmospheric gravity waves (AGWs) into the southern hemisphere, resulting in higher post-sunset plasma irregularities at southern low latitudes.

The distribution and density of plasma are affected by the changes in ionospheric electric fields and currents resulting from DD electric field caused by storm-time neutral winds and PPEF of magnetospheric origin (Astafyeva et al., 2018). Figure 11 (a-d) depicts the temporal fluctuations of the PPEF during geomagnetic storms on March 22-25, 2023, April 22-25, 2023,
330 November 4-7, 2023, and May 10-12, 2024. At 18:00 UT during the main phase of the March 23 storm, a westward PPEF of magnitude -0.55 mV/m was seen in the Asian sector. At the same time, an eastward PPEF of around 0.5 mV/m can be observed in the American and African sectors before dusk. Following sunset on April 23, multiple PPEFs of variable duration are visible in the three sectors. In America, the four PPEFs are noticeable. The first peak value is 0.33 mV/m from 18:05 to 20:05 UT, the second is -0.78 mV/m from 18:05 to 20:05 UT, the third is 0.61 mV/m from 23:05 to 23:55 UT, and the fourth
335 is 0.45 mV/m from 00:40 to 03:15 UT. In the African sector, two PPEFs of varied duration with maximum values of roughly 0.60 mV/m and -0.65 mV/m are observed before midnight from 21:00 UT to 23:00 UT and 23:05 to 23:55 UT. A strong long-duration westward PPEF with a peak value of around -1.36 mV/m is also detected after midnight, between 1:45 and 4:35 UT. In Asia, the first westward PPEF with a peak value of -0.54 mV/m occurs from 18:05 to 20:05 UT, the second eastward is 0.94 mV/m from 21:10 to 23:00 UT, and the third long duration eastward PPEF with a peak value of 0.66 mV/m occurs from
340 01:45 to 04:35 UT on April 24. During the main phase of November 4-7, 2023 storm, the PPEFs of different polarities and duration reach the equatorial ionosphere during the day. In America, the first westward PPEF with maximum value of about -0.32 mV/m occurred in the morning hours from 8:30 to 10:25 UT, and the second eastward penetrating field of magnitude about 0.44 mV/m is observed around the noon from 12:05 UT to 13:25 UT. In Africa, two noticeable PPEFs with peak values

of -0.53 mV/m and 0.34 mV/m are observed around noon. In Asia, there is one noticeable westward penetrating field with a
peak value of -0.42 mV/m from 12:05 to 13:35 UT. During mother's day geomagnetic storm on May 10–12, 2024, we observe
significant storm-time PPEFs after sunset. For instance, intense eastward-directed PPEFs of different durations between 18:00
and 22:00 UT causes super fountain effect in the American sector. This results in to a notable variations in ionospheric electron
density and the positioning of EIA crests as shown in madrigal TEC maps. We can also see eastward penetrating electric fields
with maximum values of 2.59 mV/m and 1.80 mV/m in Africa and Asia, respectively, and westward PPEF with a peak value
of roughly -2.73 mV/m in America between 22:50 and 23:25 UT. America and Africa experience an eastward PPEF with a
peak value of 1.39 mV/m and a westward PPEF with a peak value of -1.95 mV/m, respectively, between 23:30 and 2:00 UT.
During the March 23-25, 2023 storm, a westward PPEF of -0.55 mV/m was observed in the Asian sector at 18:00 UT, while
an eastward PPEF of 0.5 mV/m was seen in the American and African sectors before dusk. These PPEFs contributed to the
merging of EIA crests and increased TEC in the equatorial zone, leading to strong post-sunset plasma irregularities in the
American sector. The April 23-25, 2023 storm exhibited multiple PPEFs of varying magnitudes and durations across different
sectors, with significant eastward and westward PPEFs in America, Africa, and Asia. These PPEFs influenced the expansion of
EIA crests and increased TEC, particularly in the northern hemisphere, and caused noticeable post-sunset plasma irregularities
in the American sector. The November 4-6, 2023 storm had PPEFs of different polarities and durations, with westward and
eastward PPEFs observed in America, Africa, and Asia. However, lower ionospheric conductivity and weak electric fields
suppressed post-sunset plasma irregularities across all sectors. The May 10-13, 2024 storm featured intense eastward-directed
PPEFs between 18:00 and 22:00 UT, causing the super fountain effect in the American sector, leading to significant TEC
variations and poleward shifting of EIA crests. Strong eastward and westward PPEFs were also observed in Africa and Asia,
contributing to enhanced post-sunset plasma irregularities, particularly in the southern low latitude stations.

4 Conclusions

The comprehensive analysis of the geomagnetic storms from March 23-25, April 23-25, November 4-6, 2023, and May 10-13,
2024, reveals that solar wind parameters, geomagnetic activity, JH, and PPEFs significantly influence ionospheric TEC varia-
tions, EIA crest formations, and post-sunset plasma irregularities. Each storm exhibited unique patterns of TEC changes, driven
by the intensity and duration of geomagnetic disturbances and JH distribution. The storms also highlighted the importance of
inter-hemispheric asymmetries in JH, which affected the distribution and magnitude of ionospheric disturbances. Recom-
mendations include enhancing monitoring and predictive models for solar wind and geomagnetic activity to better anticipate
ionospheric responses, improving communication and navigation systems' resilience to geomagnetic storms, and conducting
further research on the mechanisms driving inter-hemispheric asymmetries and their impact on ionospheric dynamics.

Table 3. Joule Heating (JH), and the Equatorial Ionization Anomaly (EIA) during the main phase of the four geomagnetic storms after sunset, from 18:00 UT to 00:00 UT.

Storm Days	Time (UT)	JH(mW/m^2) Northern Hemisphere	JH(mW/m^2) Southern Hemisphere	EIA structure and Ionization level
March 23, 2023	18:00 UT	41.3	41.8	merged or single crest (moderate)
–	19:00 UT	40.7	40.7	merged or single crest (strong)
–	20:00 UT	50.9	52.6	merged or single crest (strong)
–	21:00 UT	52.5	53.4	merged or single crest (strong)
–	22:00 UT	50.1	52.0	merged or single crest (strong)
–	23:00 UT	52.2	53.9	double crest (moderate)
March 24, 2023	00:00 UT	56.6	55.9	double crest (moderate)
April 23, 2023	18:00 UT	33.7	22.9	double crest (moderate)
–	19:00 UT	94.7	77.4	double crest (strong)
–	20:00 UT	97.0	85.4	double crest (strong)
–	21:00 UT	73.5	52.2	double crest (strong)
–	22:00 UT	44.7	14.4	double crest (strong)
–	23:00 UT	55.1	24.6	double crest (moderate)
April 24, 2023	00:00 UT	37.0	13.2	double crest (weak)
November 4, 2023	18:00 UT	26.4	24.3	merged or single crest(weak)
–	19:00 UT	30.1	27.7	merged or single crest (weak)
–	20:00 UT	27.9	25.6	merged or single crest (weak)
–	21:00 UT	22.4	22.0	merged or single crest (weak)
–	22:00 UT	25.2	26.0	double crest (weak)
–	23:00 UT	25.0	28.0	double crest (weak)
November 5, 2023	00:00 UT	10.3	19.7	double crest (weak)
May 10, 2024	18:00 UT	63.8	51.8	double crest (moderate)
–	19:00 UT	47.7	30.4	double crest (moderate)
–	20:00 UT	83.1	80.9	double crest (strong)
–	21:00 UT	74.5	80.2	double crest (strong)
–	22:00 UT	114.7	101.4	double crest (strong)
–	23:00 UT	57.1	73.2	double crest (strong)
May 11, 2024	00:00 UT	98.5	116.2	double crest (weak)

375 experiments4/2021/gps/). Global ROTI maps are available at https://stdb2.isee.nagoya-u.ac.jp/GPS/GPS-TEC/. ROTI variations videos are obtained from System for Ionosphere Monitoring and Research from GNSS database, at (https://simurg.iszf.irk.ru/create_map). Equatorial electric fields over a specific longitude are obtained from the real-time Prompt Penetration Equatorial Electric Field Model (PPEEFM) available at https://geomag.colorado.edu/real-time-model-of-the-ionospheric-electric-fields.html. Weimer model Simulations are provided by the Community Coordinated Modeling Center (CCMC) at NASA Goddard Space Flight Center through (https://ccmc.gsfc.nasa.gov/
380 models/).

*Competing interests.* It is declare that the authors have no competing interest.

References

Aa, E., Zhu, S., and Liu, S.: Statistical Analysis of Equatorial Plasma Irregularities Retrieved From Swarm 2013–2019 Observations., J. Geophy. Res., 125, 2020.

385 Aarons, J.: The role of the ring current in the generation or inhibition of equatorial F layer irregularities during magnetic storms., Radio Sci., 26, 1131–1149, 1991.

Aarons, J.: Global positioning system phase fluctuations at auroral latitudes., Geophys. Res.: Space Phys., 102, 17 219–17 231, 1997.

Abdu, M. A.: Major phenomena of the equatorial ionosphere-thermosphere system under disturbed conditions., Atmospheric and Solar-Terrestrial Physics, 59, 1505–1519, 1997.

390 Abdu, M. A.: Chapter 12 - Equatorial F region irregularities, in: The Dynamical Ionosphere, edited by Materassi, M., Forte, B., Coster, A. J., and Skone, S., pp. 169–178, Elsevier, https://doi.org/https://doi.org/10.1016/B978-0-12-814782-5.00012-1, 2020.

Abdu, M. A., Batista, I. S., Reinisch, B. W., Souza, J. R. D., Sobral, J. H. A., Pedersen, T. R., Medeiros, A. F., Schuch, N. J., Paula, E. R. D., and Groves, K. M.: Conjugate Point Equatorial Experiment (COPEX) campaign in Brazil: Electrodynamics highlights on spread F development conditions and day-to-day variability, Journal of Geophysical Research: Space Physics, 114, 2009.

395 Appleton, E.: Two Anomalies in the Ionosphere., Nature, 157, 1946.

Astafyeva, E., Zakharenkova, I., Hozumi, K., Alken, P., Coïsson, P., Hairston, M. R., and Coley, W. R.: Study of the Equatorial and Low-Latitude Electrodynamic and Ionospheric Disturbances During the 22-23 June 2015 Geomagnetic Storm Using Ground-Based and Space-borne Techniques, J Geophys Res Space Phys., 123, 2424–2440, https://doi.org/10.1002/2017JA024981, 2018.

Axford, W. I.: Viscous interaction between the solar wind and the earth's magnetosphere, Planetary and Space Science, 12, 45–53,

400 https://doi.org/https://doi.org/10.1016/0032-0633(64)90067-4, 1964.

Balan, N., Alleyne, H., Otsuka, Y., Lekshmi, D. V., Fejer, B. G., and McCrea, I.: Relative effects of electric field and neutral wind on positive ionospheric storms., Earth, Planets and Space, 61, 2009.

Balan, N., Otsuka, Y., Nishioka, M., Liu, J. Y., and Bailey, G. J.: Physical mechanisms of the ionospheric storms at equatorial and higher latitudes during the recovery phase of geomagnetic storms., Journal of Geophysical Research: Space Physics, 118(5),

405 https://doi.org/https://doi.org/10.1002/jgra.50275, 2013.

Balan, N., Maruyama, T., Patra, A. K., and Narayanan, V. L.: A minimum in the latitude variation of spread-F at March equinox., Progress in Earth Planetary Sci., 5, 1–8, 2018.

Basu, S., Groves, K. M., Quinn, J. M., and Doherty, P.: A comparison of TEC fluctuations and scintillation at ascension island., J. Atmos. Solar Terr. Phys., 61, 1219–1226, 1999.

410 Blanc, M. and Richmond, A. D.: The ionospheric disturbance dynamo., Geophys. Res., 85, 1980.

Buonsanto, M. J.: Ionospheric storms:A review., Space Sci. Rev., 88, 563–601, 1999.

Calabia, A., Imtiaz, N., Altadill, D., Yasyukevich, Y., Segarra, A., Prol, F. S., Adhikari, B., del Peral, L., Frias, M. D. R., and Molina, I.: Uncovering the Drivers of Responsive Ionospheric Dynamics to Severe Space Weather Conditions: A Coordinated Multi-Instrumental Approach., Journal Geophysical Research: Space Physics, 129 (3), e2023JA031 862, https://doi.org/https://doi.org/10.1029/2023JA031862,

415 2024.

Dugassa, T., Habarulema, J. B., and Nigussie, M.: Longitudinal variability of occurrence of ionospheric irregularities over the American, African and Indian regions during geomagnetic storms., Adv. Space Res., 63, 2609–2622, 2019.

Dungey, J. W.: Interplanetary Magnetic Field and the Auroral Zones, Phys. Rev. Lett., 6, 47–48, https://doi.org/10.1103/PhysRevLett.6.47, 1961.

420 Fejer, B. G., Scherliess, L., and de Paula, E. R.: Effects of the vertical plasma drift velocity on the generation and evolution of equatorial spread F., Geophys. Res., 104, 19 854–19 869, 1999.

Fuller-Rowell, T. J., Codrescu, M. V., Moffett, R. J., and Quegan, S.: Response of the Thermosphere and Ionosphere to Geomagnetic Storms., Geophysical Research, 99, 3893–3914, 1994.

Fuller-Rowell, T. J., Codrescu, M. V., Roble, R. G., and Richmond, A. D.: How does the thermosphere and ionosphere react to a geomagnetic
425 storm?, Geophysical monograph series, 98, 203–225, 1997.

González, G.: Storm-time variability of ionospheric irregularities over South America., Atmospheric and Solar-Terrestrial Physics, 241, 105 980, https://doi.org/https://doi.org/10.1016/j.jastp.2022.105980, 2022.

H Jin, C Yan, G. Y. F. H. H. X. X. Z. W. S. Y. L. K. H. J. J.: Interaction Between Equatorial to Low-Latitude Postmidnight F-Region Irregularities and LSTIDs in China During Geomagnetic Disturbances Based on Ground-Based Instruments., JGR, 127(6), 2022.

430 Huang, C. S.: Long-Lasting Penetration Electric Fields during Geomagnetic Storms: Observations and Mechanisms, Geophysical Research, 124, 2019.

Huang, C. S., Foster, J., and Michael, K.: Long-duration penetration of the interplanetary electric field to the low-latitude ionosphere during the main phase of magnetic storms, Geophysical Research, 110, 2005.

Huang, L., Huang, J., Wang, J., Jiang, Y., Deng, B., Zhao, K., and Lin, G.: Analysis of the north–south asymme-
435 try of the equatorial ionization anomaly around 110°E longitude, Atmospheric and Solar-Terrestrial Physics, 102, 354–361, https://doi.org/https://doi.org/10.1016/j.jastp.2013.06.010, 2013.

Imtiaz, N., Dugassa, T., Calabia, A., Anorou, C., and Kashcheyev, A.: Westward PPEF plays important role in the suppression of post-midnight plasma irregularities: A case study of the November 2021 geomagnetic storm., Journal Geophysical Research: Space Physics, 129, e2023JA032 367, https://doi.org/https://doi.org/10.1029/2023JA032367, 2024.

440 Kassa, T., Damtie, B., Bires, A., Yizengaw, E., and Cilliers, P.: Storm-time characteristics of the equatorial ionization anomaly in the East African sector., Advances in Space Research, 56, 57–70, https://doi.org/https://doi.org/10.1016/j.asr.2015.04.002, 2015.

Kassa, Y., Damtie, B., and Tebabal, A.: Ionospheric and magnetic signatures of extreme space weather events of 17 March and 23 June 2015 over the African sector., Atmospheric and Solar-Terrestrial Physics, 243, 106 003, 2023.

Kassa, Y., Tebabal, A., and Damtie, B.: Nighttime ionospheric irregularity during intense geomagnetic storm events over the Europe-African
445 longitudinal sector., Heliyon, 10, e38 138, 2024.

Kelly, M. C.: The Earth's Ionosphere: Plasma Physics and Electrodynamics, Second Edition, 2009.

Kikuchi, T., Hashimoto, K. K., and Nozaki, K.: Penetration of magnetospheric electric fields to the equator during a geomagnetic storm., Geophys. Res., 113, 2008.

Li, K. F., Lin, L. C., and Bui, X H andLiang, M. C.: The 11 year solar cycle response of the equatorial ionization anomaly observed by GPS
450 radio occultation, Journal of Geophysical Research: Space Physics, 123, https://doi.org/10.1002/2017JA024634, 2018.

Lin, C. H., Richmond, A. D., Heelis, R. A., Bailey, G. J., Lu, G., Liu, J. Y., and Su, S. Y.: Theoretical study of the low- and midlatitude ionospheric electron density enhancement during the October 2003 superstorm: Relative importance of the neutral wind and the electric field, Journal of Geophysical Research, 110, https://doi.org/doi.org/10.1029/2005JA011304, 2005.

Lukianova, R.: Swarm field-aligned currents during a severe magnetic storm of September 2017, Annales Geophysicae, 38, 191–206,
455 https://doi.org/10.5194/angeo-38-191-2020, 2020.

M, C., S, M., A, C., and Sardon, E.: Characterization of equatorial ionospheric features on the verge of the next solar cycle maximum., p. 3055–3065, https://doi.org/https://doi.org/10.1029/2004JA010884, 2012.

Pi, X., Mannucci, A., Lindqwister, U. J., and Ho, C. M.: Monitoring of global ionospheric irregularities using the worldwide GPS network., Geophys. Res. Lett., 24, 2283–2286, 1997.

460 Richmond, A. D. and Matsushita, S.: Thermospheric Response to a Magnetic Substorm., Geophys. Res., 80 (19), 2839–2850, 1975.

Rideout, W. and Coster, A.: Automated GPS processing for global total electron content data., GPS Solutions, 10, 219–228, 2006.

Rishbeth, H.: The equatorial F-layer: progress and puzzles, Annales Geophysicae, 18, 730–739, https://doi.org/10.1007/s00585-000-0730-6, 2000.

Seemala, G.: GPS-TEC analysis application., Technical Report. Tech. Rep., Inst. for Sci. Res., USA, 2011.

465 Smith, A. R., Ozturk, D. S., Delamere, P., Lu, G., and Kim, H.: Investigating the interhemispheric asymmetry in Joule heating during the 2013 St. Patrick's Day geomagnetic storm., Space Weather, 21, e2023SW003 523, 2023.

Tahir, A., Wu, F., Shah, M., Amory-Mazaudier, C., Jamjareegulgarn, P., Verhulst, T. G. W., and Ameen, M. A.: Multi-Instrument Observation of the Ionospheric Irregularities and Disturbances during the 23–24 March 2023 Geomagnetic Storm, Remote Sensing, 16, https://www.mdpi.com/2072-4292/16/9/1594, 2024.

470 Tsurutani, B., Mannucci, A., Iijima, B., Abdu, M. A., Sobral, J. H. A., Gonzalez, W., Guarnieri, F., Tsuda, T., Saito, A., Yumoto, K., Fejer, B., Fuller-Rowell, T. J., Kozyra, J., Foster, J. C., Coster, A., and Vasyliunas, V. M.: Global dayside ionospheric uplift and enhancement associated with interplanetary electric fields., Geophys. Res., 109, 2004.

Tulasi, R., Su, S. Y., and Liu, C. H.: FORMOSAT-3/COSMIC observations of seasonal and longitudinal variations of equatorial ionization anomaly and its interhemispheric asymmetry during the solar minimum period., Geophys. Res., 114 (A6), 475 https://doi.org/https://doi.org/10.1029/2008JA013880, 2009.

Vaggu, P. R., Deshpande, K. B., Datta-Barua, S., Bust, G. S., Hampton, D. L., Rubio, A. L., and Conroy, J. P.: Morphological and Spectral Features of Ionospheric Structures at E- and F-Region Altitudes over Poker Flat Analyzed Using Modeling and Observations, Symmetry, 15, https://doi.org/10.3390/sym15101940, 2023.

Weimer, D. R.: Improved ionospheric electrodynamic models and application to calculating Joule heating rates, J. Geophysical Research, 480 110, A05 306, https://doi.org/https://doi.org/10.1029/2004JA010884, 2005.

Wu, K., Qian, L., Wang, W., Cai, X., and Mclnerney, J. M.: Investigation of the GOLD observed merged nighttime EIA with WACCM-X simulations during the storm of 3 and 4 November 2021, Geophys. Res. Lett., 50, https://doi.org/10.1029/2023GL103603, 2023.

Zhang, Y., Liu, Y., Mei, J., Zhang, C., and Wang, J.: A Study on the Characteristics of the Ionospheric Gradient under Geomagnetic Perturbations, Sensors, 20, https://www.mdpi.com/1424-8220/20/7/1805, 2020.
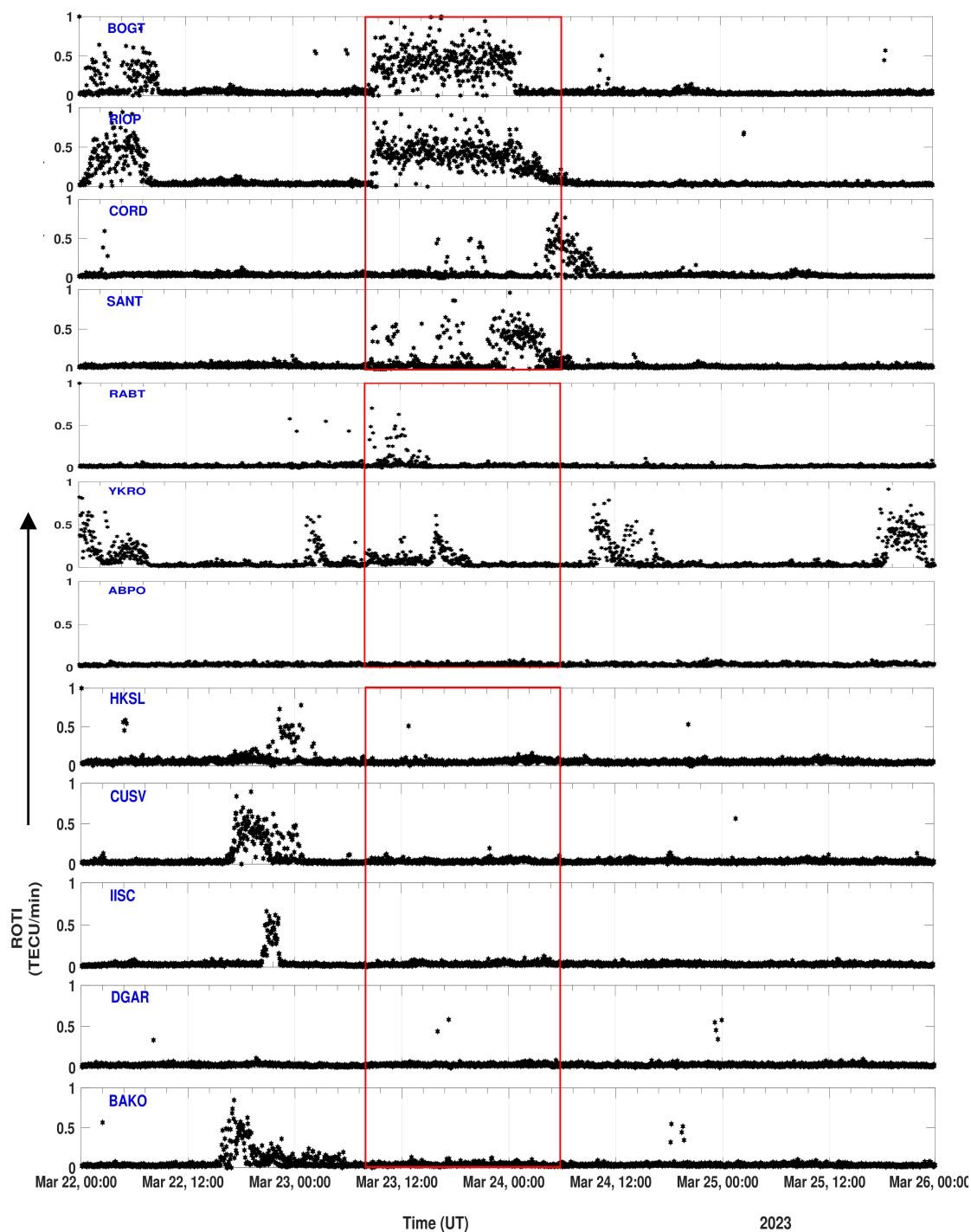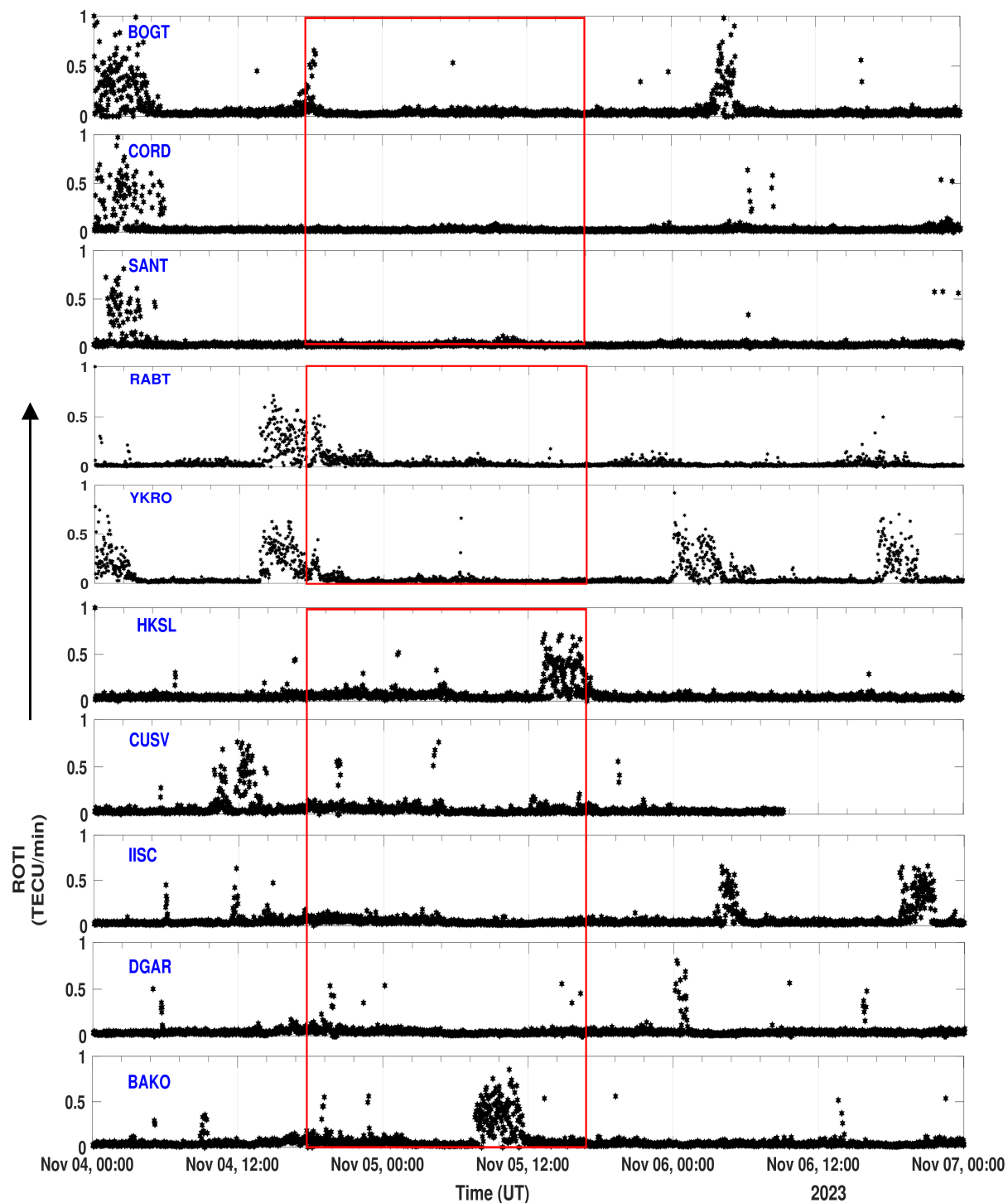
Figure 7. Temporal variation of ionospheric ROTI during March 22-25, 2023.
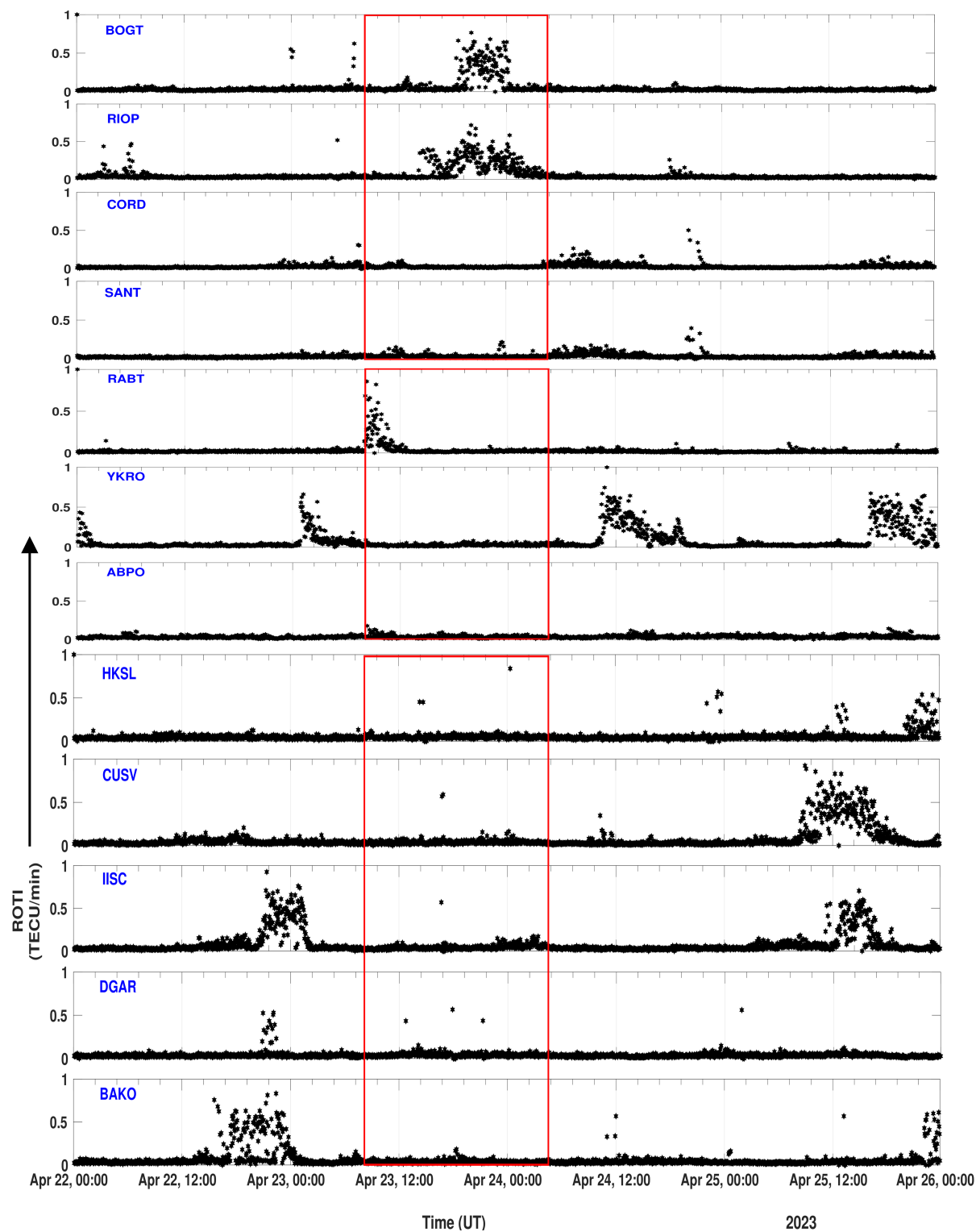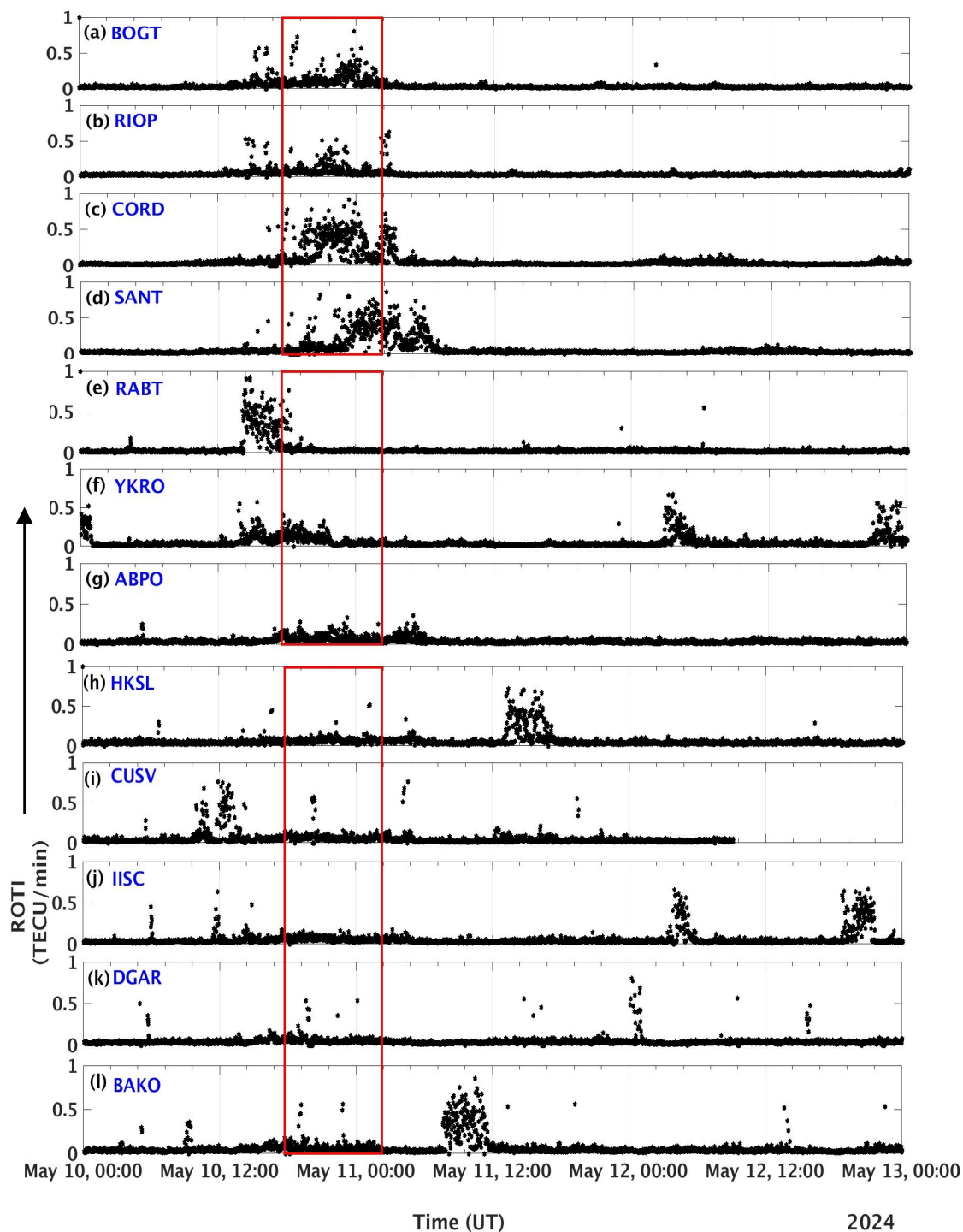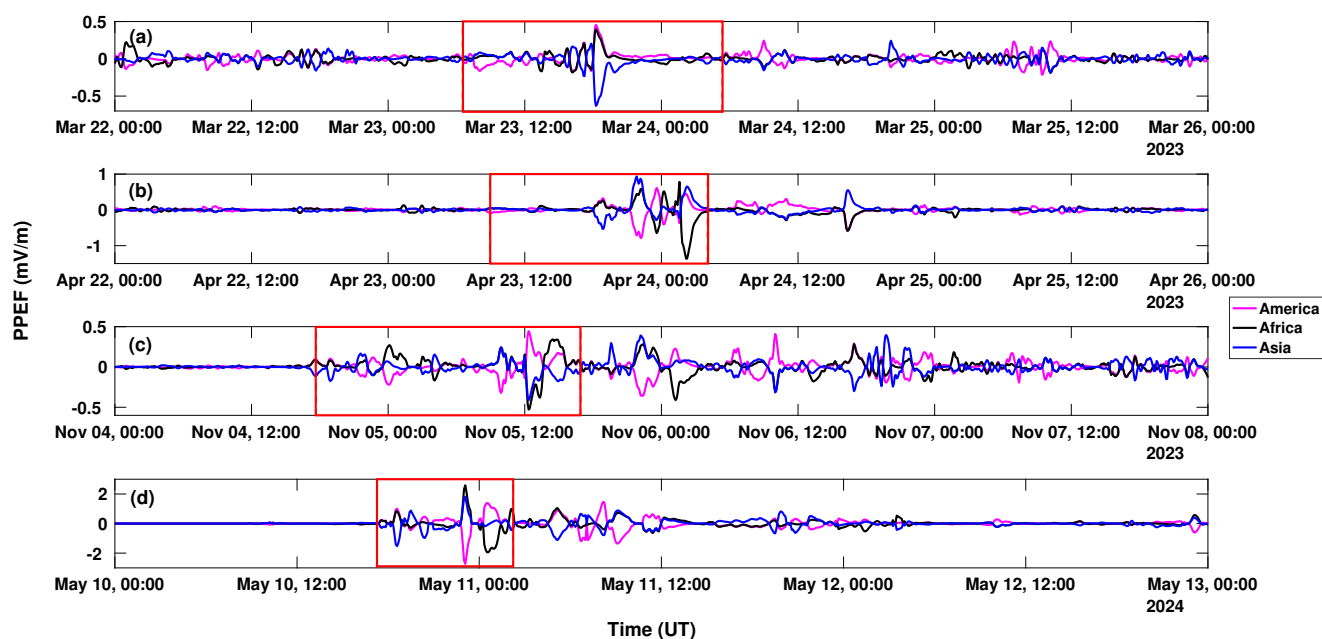
Figure 8. Temporal variation of ionospheric ROTI during April 22-25, 2023.

Figure 9. Temporal variation of ionospheric ROTI during November 4-7, 2023.

Figure 10. Temporal variation of ionospheric ROTI during May 10-13, 2024.

Figure 11. Variations in the ionospheric prompt penetration electric fields (PPEFs) over the three longitudes during the three intense geomagnetic storms of SC 25.